Improved Oxidation and Hot Corrosion Resistance of 1Cr11Ni2W2MoV Stainless Steel at 650 °C by a Novel Glass-Ceramic Coating

Ken Chen [1], Jiewei Lin [1], Wenfang Li [1,*], Wen Zhu [1], Kang Li [1], Aihua Yi [1], Shaodong Hu [1], Minghui Chen [2] and Fuhui Wang [2]

[1] School of Materials Science and Engineering, Dongguan University of Technology, 1 Daxue Rd, Dongguan 523808, China; chenk@dgut.edu.cn (K.C.); lin15016319985@163.com (J.L.); zhuwen@dgut.edu.cn (W.Z.); shdlikang@163.com (K.L.); yiaihua92751@163.com (A.Y.); hushao2009@foxmail.com (S.H.)

[2] Shenyang National Laboratory for Materials Science, School of Materials Science and Engineering, Northeastern University, Shenyang 110819, China; mhchen@mail.neu.edu.cn (M.C.); fhwang@mail.neu.edu.cn (F.W.)

* Correspondence: liwenfang@dgut.edu.cn; Tel.: +86-769-2286-2966

Abstract: A novel glass-ceramic coating was applied onto the 1Cr11Ni2W2MoV stainless steel. The oxidation and corrosion behaviors of coated and uncoated steels were comparatively investigated in air and in the presence of NaCl + Na$_2$SO$_4$ eutectic deposits at 650 °C, respectively. Protective scales formed on the surface of stainless steel prevented the severe oxidation of the alloy. Catastrophic hot corrosion occurred on the steel when a salt film was attached, producing loose iron oxide layers and internal corrosion zone. The glass-ceramic coating acted as a barrier that effectively hindered the invasion of corrosive species during the oxidation and hot corrosion tests.

1. Introduction

Martensitic stainless steel (MSS for short) is widely used in turbine blades, discs, and other high-temperature parts due to its high temperature oxidation resistance and mechanical properties at high temperatures [1]. The high content of Cr in the alloy is beneficial for the formation of a protective Cr$_2$O$_3$ layer at high temperatures [2,3]. At the same time, due to the addition of W, Mo and V, which can react with carbon to form dispersed precipitate, satisfactory comprehensive mechanical properties can be obtained [4]. However, sulfur in fuel and chlorine in marine environments trend to deposit on the surface of the component and form a salt film, which will cause serious hot corrosion invasion on the surface of the MSS [5–9].

One of the most effective ways to improve the hot corrosion resistance of alloys is to apply a high temperature protective coating on the alloy surface. The metal coating (such as NiCrAlY) can combine with the substrate, but its hot corrosion resistance is still not satisfactory [10,11]. Ceramic coatings have high chemical stability, but they are easy to peel off in cold and hot cycles because of the large gap of the thermal expansion coefficient (CTE for short) between the coating and the substrate [12–14].

Recently, glass-ceramic coatings (GCC for short) have attracted attention due to their simple preparation process, adjustable CTE in a wide range, and chemical inertness at high temperatures [15–21]. Wenbo Li et al. developed an oxidation resistant GCC on Ti-47Al-2Cr-2Nb alloy, which decreased the oxidation rate of the alloy significantly at 900 °C [22]. Minghui Chen et al. found that GCC could provide effective protection for Ti-6Al-4V alloy against high temperature oxidation at 800 °C [23]. A GCC was prepared on

the surface of TiAl by Yimin Liao et al., protecting against oxidation under thermal shock in NaCl solution [24].

However, MSS has a higher CTE than titanium alloy. The above mentioned GCC may peel off due to the excessive CTE mismatch between the coating and substrate. Moreover, in order to achieve excellent mechanical properties, MSS is often heat-treated with quenching at 1000–1050 °C and then tempering at 720–800 °C [25]. In order to retain tempered martensite with excellent mechanical properties, the coating should be sintered at a relatively low temperature. However, the firing temperatures of the reported high temperature protective GCC systems [15–24] are well above 800 °C, which is much higher than the tempering temperature of the MSS and are harmful to its mechanical properties. Therefore, it is very important to redesign a GCC with suitable CTE and firing temperature for MSS.

A popular way to elevate the CTE and reduce the firing temperature of glass is to increase the content of alkali metal oxides [26]. However, an excessive introduction of fluxes will seriously damage the silica network of glass, resulting in poor high temperature protection performance of the coating. By introducing a variety of alkaline earth metals, the CTE of glass can be improved, and glass can also be strengthened by the precipitation of crystals at high temperatures [27].

In the present work, a new type of SiO_2-Al_2O_3-Q_2O-RO (Q = Na and K; R = Mg, Ca and Ba) GCC was designed to enhance the oxidation and corrosion inhibition of MSS. The oxidation and hot corrosion mechanisms of MSS were discussed. In addition, the crystallization behavior of the GCC with and without $NaCl$-Na_2SO_4 molten eutectic salt attachment at 650 °C was studied in detail.

2. Material and Methods

2.1. Coating Preparation

1Cr11Ni2W2MoV MSS (Hongyongchang Metal Material Co., Ltd, China) was used as the substrate. The nominal composition (wt.%) of MSS is: C: 0.1–0.16%; Cr: 10.5–12.0%; Ni: 1.4–1.8%; W: 1.5–2.0%; Mo: 0.35–0.5%; V: 0.18–0.3%; Si $\leq$ 0.6%; Mn $\leq$ 0.6%; S $\leq$ 0.02%; P $\leq$ 0.03%; Fe: Bal. The cylindrical specimens with dimension of $\Phi 25 \times 2.5$ mm were successfully ground, polished, and cleaned with acetone in an ultrasonic cleaner.

The nominal composition (wt.%) of GCC is: SiO_2: 67.5%; Na_2O: 12.5%; Al_2O_3: 6%; K_2O: 1.5%; MgO: 1.5%; CaO: 7%; BaO: 1%. The preparation process of glass powder was as follows. First, 500 g raw materials were weighed, sealed in an agate pot, mixed by a ball mill for 30 min, and poured into a crucible. Second, the glass melt was obtained by holding for 3 h at 1250 °C. Then, glass glazes were obtained by water quenching, dried in an oven at 100 °C, and milled in agate for 100 h. Finally, the coarse glass particles were separated and removed from the glass powders by a 200-mesh sieve.

The GCC was prepared by the atmospheric spray-firing method, and the specific steps were as follows. First, the slurry was obtained by ball milling operations that were carried out in a ball milling machine, where the frit granules and ethanol (in ratio of 10 g: 120 mL), combined with agate balls, were sealed in an agate container. Second, the slurry was sprayed on the surface of MSS by spray gun. The thickness of the coating was accurately controlled by adjusting the spraying distance and spraying times. Then, the sprayed samples were put into the oven at 100 °C and dried for 10 min to obtain the biscuits. Finally, the biscuits were fired at 800 °C for 10 min in a muffle furnace.

2.2. High Temperature Oxidation Test

Intermittent oxidation was carried out in static air at 650 °C for 100 h with weight measurements performed at regular intervals. The samples were put into a crucible, immediately heated and oxidized in muffle furnace, and taken out at a certain time point. Each time, the sample was taken out and put into a drying dish to cool for 1.5 h to room temperature, before being weighed with an electronic balance (Sartorius BP211D with

precision of 0.01 mg). Three parallel samples were prepared for each process, and the average value of the three samples was taken for the kinetic curve.

2.3. Hot Corrosion Test

The hot corrosion test was carried out at 650 °C for 100 h. The experimental process was as follows:

(1) The supersaturated salt solution was prepared by adding enough eutectic salt (68 wt.% Na_2SO_4 + 32 wt.% NaCl) into deionized water at 100 °C, and then the salt solution was coated on the heated sample surface to form a salt film. The salt brushing process was repeated until the final amount of deposited salt reached 2.0 ± 0.5 mg/cm^2.

(2) All the salt coated samples were fixed on a frame, moved into the furnace, and immediately heated to 650 °C. After 20 h of hot corrosion in static air atmosphere, corroded samples were removed from the furnace and cooled to room temperature in air.

(3) The samples were washed in boiling deionized water to dissolve and remove salt and/or loose corrosion products from the surface. After being filtered by filter paper, the impure water was further heated to complete volatilization so that the dissolved corrosion products were precipitated out and then collected for component analysis. The cleaning process was carried out three times for 30 min each time, until the soluble corrosion products no longer turned deionized water yellow. After that, all the cleaned samples were taken out of the water and dried.

(4) The weight of the completely dried sample was recorded by an electronic balance. After weighing, all samples were coated with a fresh salt again to start the next corrosion cycle.

2.4. Characterization

X-ray diffraction (PANalytical X' Pert PRO, Cu Kα radiation at 40 kV, PA Analytical, Almelo, Holland) was employed to analyze the phase of the steel, GCC, and corrosion product. Surface and cross-sectional microstructures were characterized by SEM (Inspect F50; FEI, Hillsboro, OR) and EDS (X-Max; Oxford instruments, Oxford, UK).

3. Results

3.1. As-Prepared Coating

The surface morphology of the as-prepared coating is shown in Figure 1a. At a high temperature, glass particles softened and melted onto the surface of MSS, and then connected with each other to form a dense coating. The surface of the coating was very flat, but there was still a small amount of incomplete melting particles with a diameter of approximately 9 μm. Figure 1b shows the cross-section morphology of the prepared coating. The thickness of GCC was about 60 μm. The coating was compact, but there were also some bubbles with a diameter of about 2 μm, which formed during sintering. The EDS data were collected in the area of the coating surface and the related results are shown in Figure 1c,d, where the significant signals of Si, Al, Mg, Na, Ca, K, O, Ba can be detected.
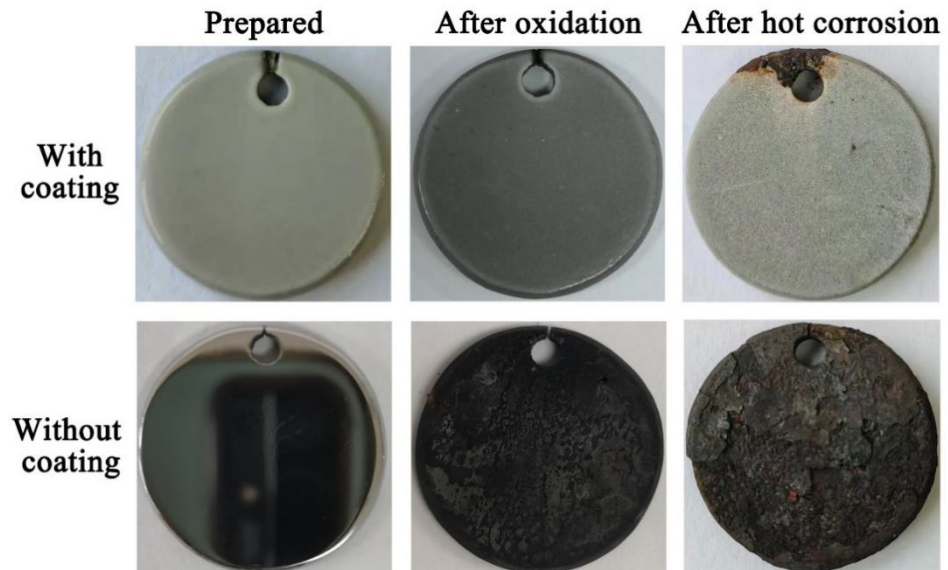
3.2. Macro-Morphology of Samples before and after Oxidation and Hot Corrosion

Figure 2 shows the macro-morphology of MSS with and without coating in the as-prepared state, after oxidation and hot corrosion for 100 h at 650 °C. When the samples with GCC were prepared, they were gray-white, smooth, and glassy. After oxidation at 650 °C for 100 h, the coating remained intact without obvious defects, but the color of the coating turned dark gray. After hot corrosion at 650 °C for 100 h, the coating became rough and lost its glass luster. It should be noted that the suspension position, located in the upper of the process hole, was difficult to cover with glass particles during spraying, leading to serious hot corrosion at this location. For MSS without coating, the polished sample looked like a mirror and was reflective. After 100 h of corrosion, a black oxide film covered the surface. In the presence of salt film, MSS was subjected to catastrophic corrosion. The corrosion

products on the surface of MSS had a multilayer structure. A large scale exfoliation of corrosion products revealed the weak connection between rust and MSS.
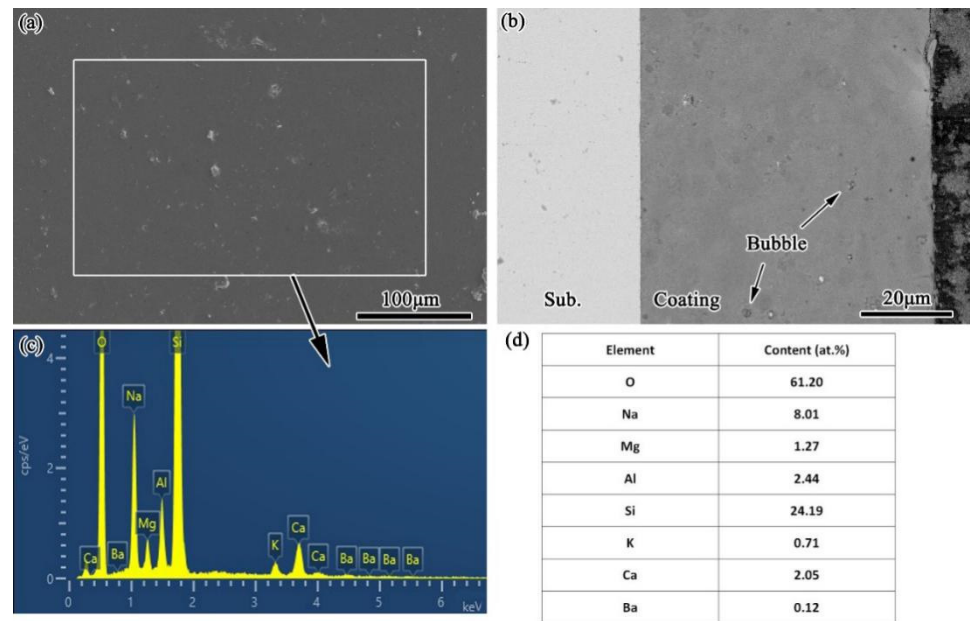
Figure 1. Surface image (**a**), cross-sectional image (**b**), and elemental profile (analyzed by EDS) (**c**,**d**) of the as-prepared GCC on MSS.


Figure 2. Macromorphology of MSS with and without GCC in as prepared state, after oxidation and hot corrosion at 650 °C for 100 h.

3.3. Intermittent Oxidation

3.3.1. Oxidation Kinetics

Figure 3 shows the intermittent oxidation kinetics of MSS with and without the GCC at 650 °C. The oxidation kinetics of MSS at this temperature basically conformed to the parabolic law, which indicated that the black oxide film observed in the macro-morphology (Figure 2) was protective at 650 °C. The parabolic rate constant of oxidation k_P was 3.51×10^{-3} mg^2/(cm^4·h), and its weight gain was 0.163 mg/cm^2 after oxidation at 650 °C for 100 h. Compared with MSS, the oxidation weight gain of the samples coated with GCC

was lower. The parabolic rate constant (k_p) of the samples was 4.19×10^{-4} mg^2/(cm^4·h), which was about an order of magnitude lower than that of bare MSS. The weight gain of the samples after oxidation for 100 h was only 0.019 mg/cm^2.
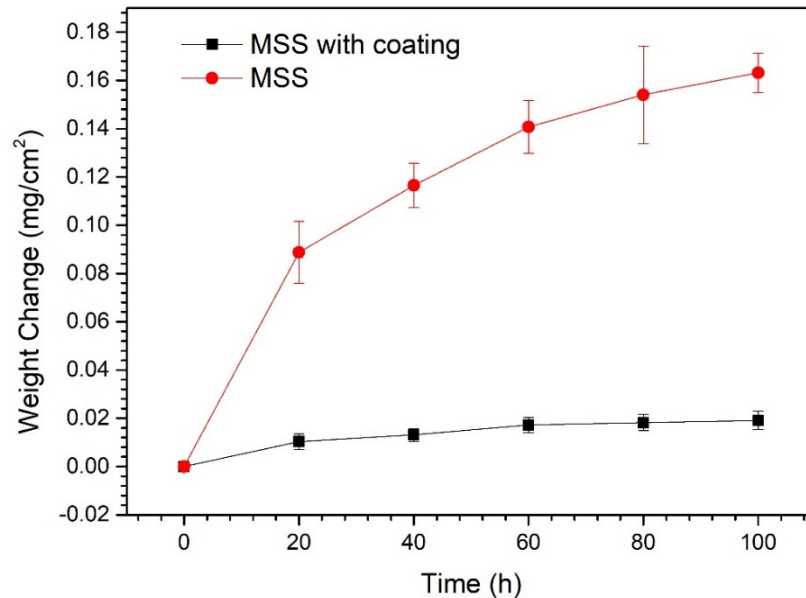
**Figure 3.** Interrupted oxidation kinetics of MSS with and without GCC at 650 °C.

3.3.2. XRD Patterns

Figure 4a shows the XRD patterns of prepared MSS and oxidized for 100 h at 650 °C. The polished substrate had strong signal peaks at 44.7°, 65° and 82.3°, which are the peaks of Fe-Cr alloy. After oxidation for 100 h, besides the above positions, peaks at 24.5°, 33.6°, 36.2°, 41.5°, 50.2°, 54.9° and 65.1°, were also found, which correspond to Cr$_2$O$_3$.

Figure 4b shows the XRD patterns of MSS with GCC in the prepared state and after oxidation at 650 °C for 100 h. In the as-prepared state, a broad peak appearing in around of 20–30° could be attributed to the existence of the amorphous phase. In addition, the peak in 20.9°, 26.6°, and 36.5°, corresponding to (100), (011), and (110) of quartz, respectively, indicated that part of the quartz precipitated from the glass phase during the sintering process. After oxidation, the peak strength of quartz increased significantly, which meant that the amount of the precipitated quartz in the coating increased significantly. The peak values of calcium silicate, barium chromate, and barium silicate were also detected.

3.3.3. Micro-Morphology

The surface microstructure of MSS after oxidation is shown in Figure 5a. An oxide film composed of flake oxide was found on its surface. An SEM image recorded at high magnification clearly shows that the growth angles of these polygonal flaky oxides were different, as shown in Figure 5b. The size of these oxide crystals ranged 4–15 μm. This morphology was consistent with that of the chromium oxide film typically observed in iron-based alloys with high chromium content at a high temperature [28,29]. The cross-section morphology (Figure 5c) showed that the oxide layer formed by the polygonal flake crystals was not dense. In order to confirm the main composition of the oxide layer, EDS analysis was carried out on the position in Figure 6c, and the surface scanning results are shown in Figure 5d. Cr and O were obviously enriched in the oxide layer, while Fe could hardly be detected. Combined with the previous XRD analysis results (Figure 4a), it was concluded that the main crystal of the oxide layer was Cr$_2$O$_3$.
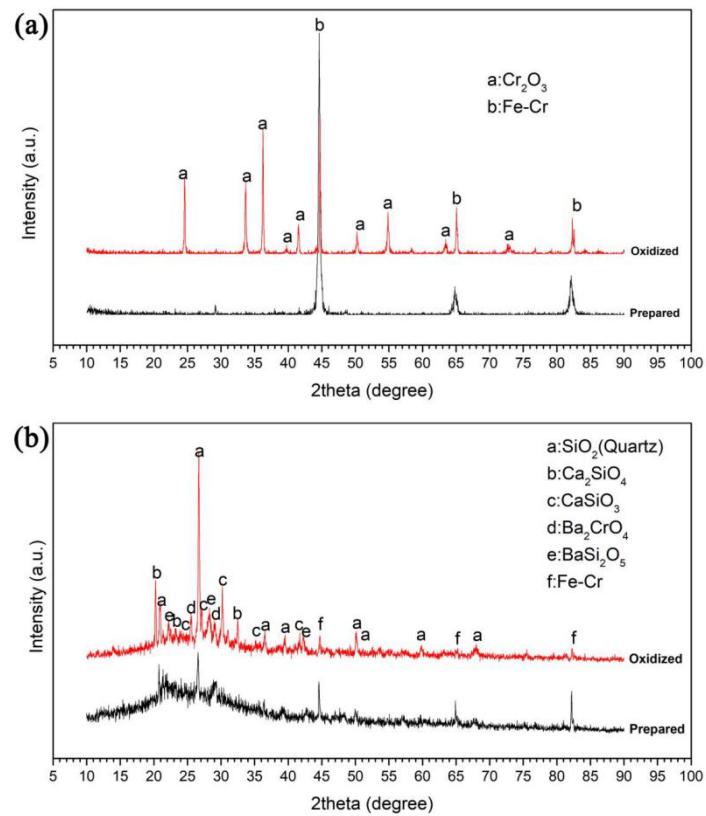
Figure 4. XRD patterns of as-prepared MSS without (**a**) and with (**b**) GCC and oxidized for 100 h at 650 °C.
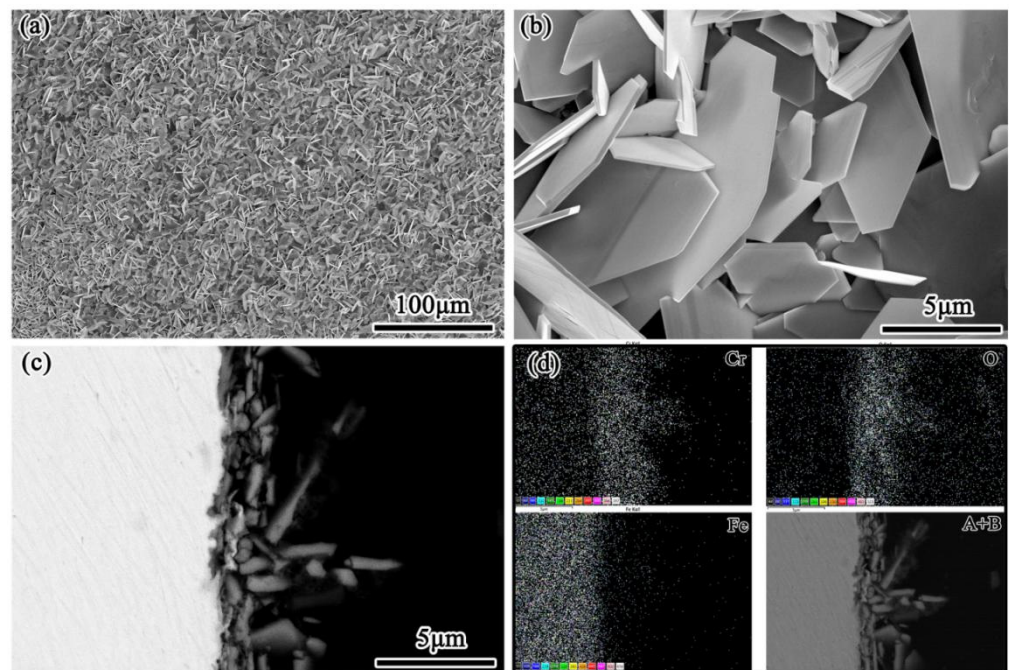
Figure 5. Low-magnification morphology (**a**), high-magnification surface image (**b**), cross-sectional image (**c**), and elemental map-scan profile (analyzed by EDS) (**d**) of the MSS after 100 h oxidation at 650 °C.
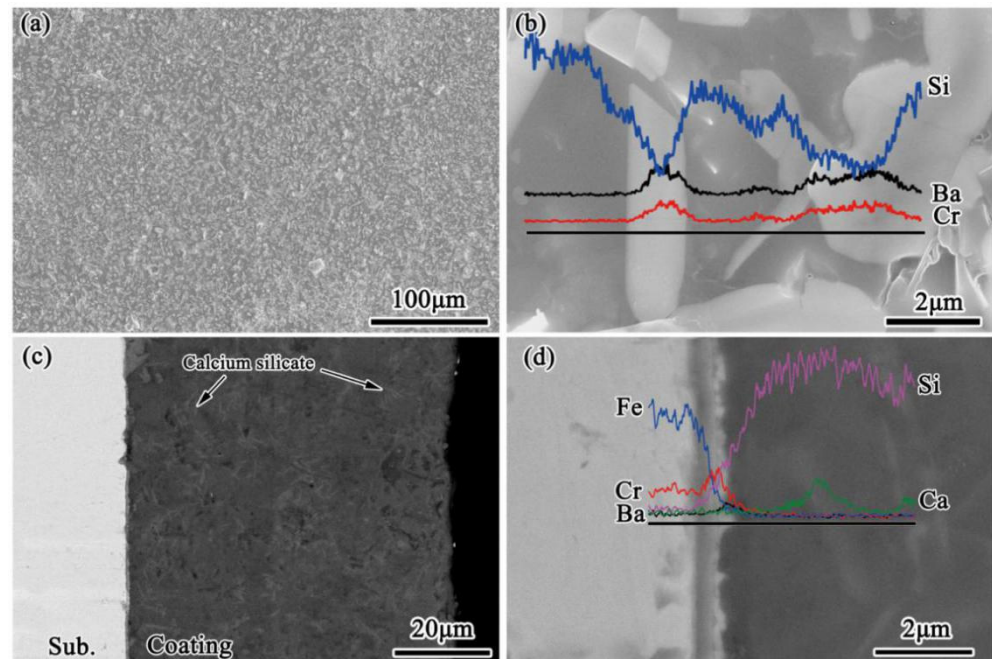
Figure 6. Low-magnification morphology (**a**), high-magnification surface image (**b**), low-magnification cross-sectional image (**c**), and high-magnification cross-sectional image (**d**) of the MSS with GCC after 100 h oxidation at 650 °C.

Figure 6a shows the surface morphology of MSS with GCC after oxidation for 100 h. A great quantity of white crystals precipitated on the surface of the coating. The composition of these crystals was analyzed by EDS, and the results are shown in Figure 6b. The content of Ba and Cr in these crystals was significantly higher than that in the surrounding glass phase, while the distribution of Si was exactly the reverse. Combining these results with those of the previous XRD analysis, it was concluded that these crystals were Ba_2CrO_4. Figure 6c shows the cross-section morphology of the coated MSS after high temperature oxidation. The thickness of the coating was basically consistent with the as-prepared state, and the coating was still dense. However, a large number of bright-white acicular crystals, with a length of 2–5 μm, were precipitated from the glass phase. According to the high magnification image and the EDS line scans (Figure 6d), a double-layer structure interface layer was formed at the interface between the coating and the substrate. The Cr content of the layer in the vicinity of the substrate was obviously enriched, whereas the layer in the vicinity of the coating was rich in Cr and Ba. It should be noted that the Ca content of the bright-white acicular crystals inside the coating was significantly higher than that of the surrounding glass phase. Combined with the XRD results of Figure 4b, it was concluded that the acicular crystal in the coating was calcium silicate. Although the XRD patterns show that a large amount of quartz precipitated in the coating, it was difficult to distinguish the quartz particles from the glass in the back-scattered electron mode because of the inconspicuous contrast between quartz and glass.

3.4. Hot Corrosion

3.4.1. Hot Corrosion Kinetics

The hot corrosion kinetics of MSS with and without the GCC at 650 °C are shown in Figure 7. Catastrophic corrosion occurred in MSS under the coverage of the molten salt film. In each corrosion cycle (20 h), the weight loss of metal was large, which was caused by the peeling of loose corrosion products during the process of removing the salt film. After 100 h of hot corrosion, the mean corrosion weight loss reached 13.85 mg/cm², with an average corrosion rate of 0.128 mg/(cm²·h). In addition, the error of the corrosion kinetics data of the MSS was large. The error was primarily due to the random peeling

of the corrosion product film caused by the impact of bubbles in boiling water during cleaning. In contrast, after 100 h of hot corrosion, the weight gain of MSS with coating was only 0.46 mg/cm^2, greatly improving the substrate's resistance to hot corrosion.
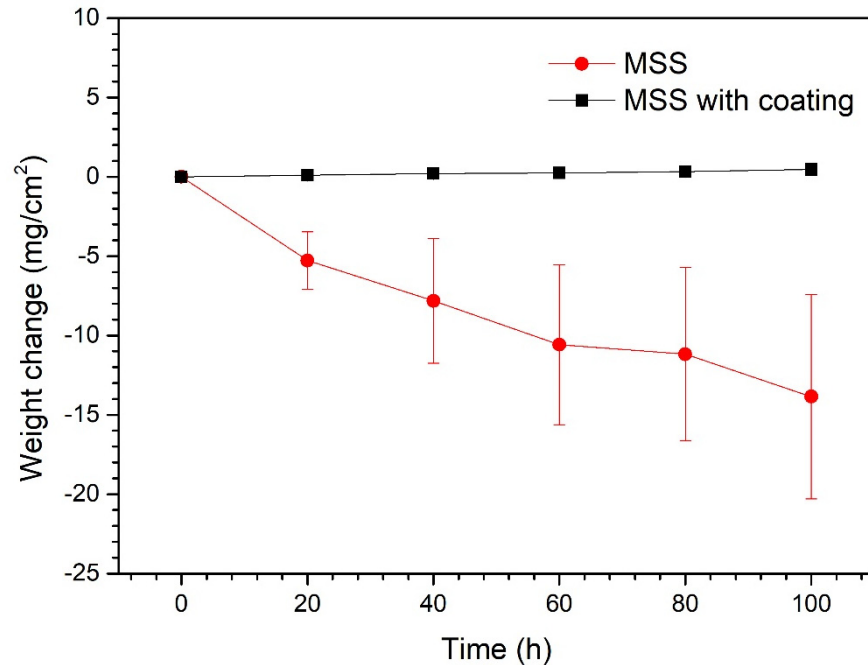

Figure 7. Hot corrosion kinetics of MSS with and without GCC at 650 °C.

3.4.2. XRD Patterns

Figure 8a shows the XRD patterns of MSS hot corrosion for 100 h at 650 °C. Unlike high temperature oxidation in air, peaks of Cr_2O_3 could not be found, but strong peaks of Fe_2O_3 and Fe_3O_4 did appear. Figure 8b shows the XRD pattern of the coating after hot corrosion. Compared with the pattern after oxidation without salt, the peaks of quartz and calcium silicate could no longer be found, but the peaks of magnesium calcium silicate and calcium sodium silicate were quite evident.

3.4.3. Micro-Morphology

The surface micro-morphology of MSS hot corrosion is shown in Figure 9a. The residual corrosion products on the surface had the characteristics of a multilayer structure. Each layer could be subdivided into two layers: the granular crystal layer and the upper layer consisting of flaky crystal. According to the results of XRD (Figure 8a), the granular crystal was inferred to be Fe_3O_4 and the flaky crystal was inferred to Fe_2O_3. There were many cracks in the corrosion product layer. The cross-section morphology of MSS hot corrosion is shown in Figure 9b. The thickness of the hot corrosion affected zone reached 90 μm. It could be divided into three zones: the outermost loose oxide layer, the metal-oxide mixed layer, and the inner corrosion zone. The porous oxide layer had a multilayer structure and many cracks, which was similar to the morphology observed on the surface. The thickness of the metal-oxide mixed layer was about 20 μm. In this layer, metals that had not been corroded were wrapped by porous oxide. There were obvious internal oxidation and internal sulfidation in the alloy with evident intergranular corrosion characteristics.
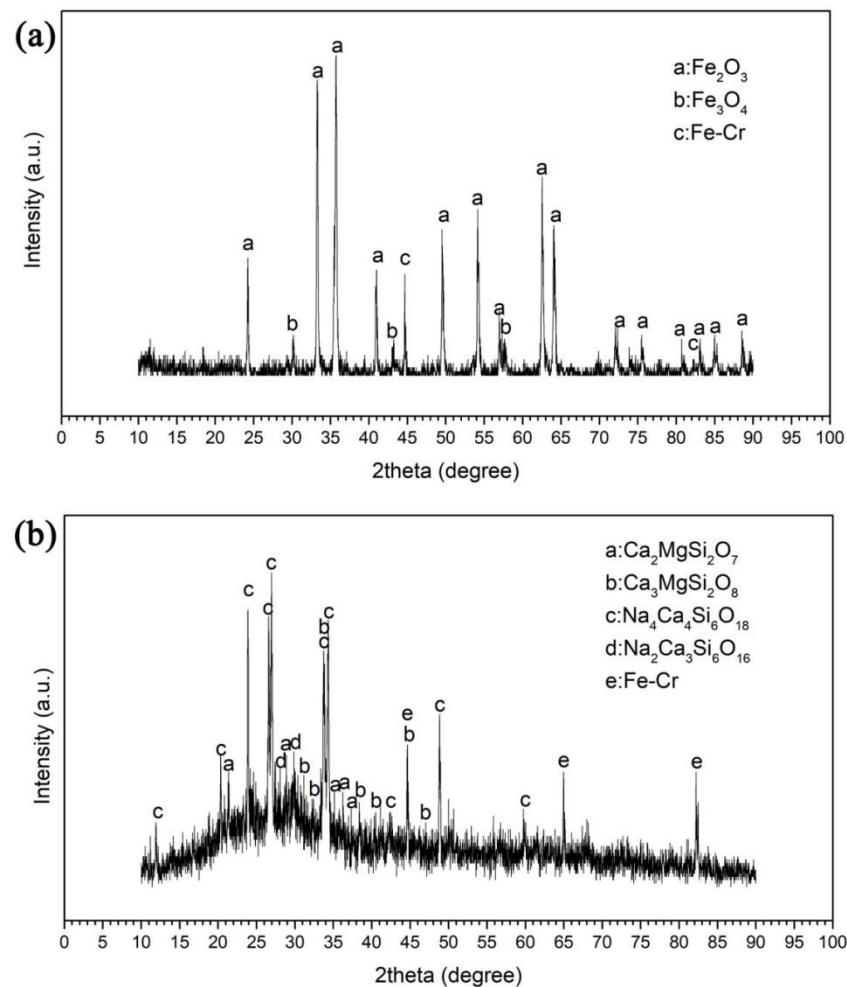
Figure 8. XRD patterns of MSS without (**a**) and with (**b**) GCC after hot corrosion for 100 h at 650 °C.
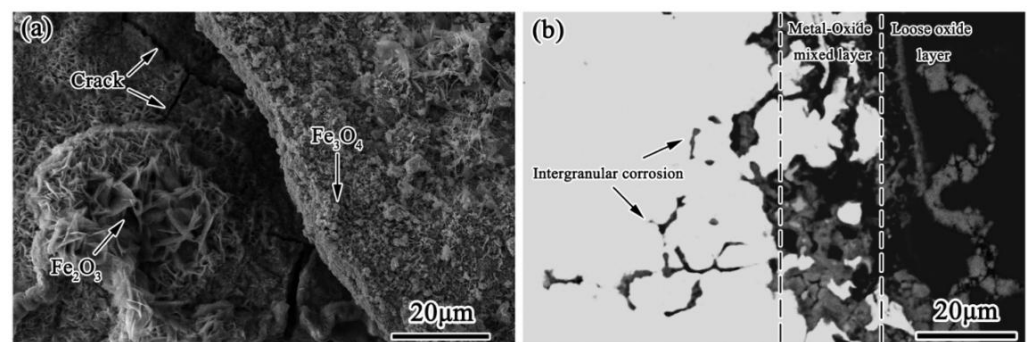

Figure 9. (**a**) Surface image and (**b**) cross-sectional image of the MSS after 100 h hot corrosion at 650 °C.

Figure 10 shows the morphology(a) and elemental profile (analyzed by EDS) of the dissolved corrosion products precipitating from cleaning water. The corrosion product crystallized in granular shape, where the significant signals of Cr, W, Na, S, and Cl could be detected.

The surface morphology of the coating after hot corrosion is shown in Figure 11a. After hot corrosion and boiling, the surface of the GCC became rougher than that of the oxidized coating, and abundant crystals were precipitated. SEM image recorded at high magnification (Figure 11b) clearly showed that the surface was mainly composed of two kinds of crystals with different morphologies (sword and needle) and partially dissolved

glass. The width of the sword crystal was about 5 μm and the length was about 20 μm. The length of acicular crystal was about 15 μm. EDS was used to analyze the composition of the area, and the results are shown in Figure 11c. The sword crystals were enriched with magnesium, and the content of sodium in these areas was relatively low. In contrast, the acicular crystals were in a sodium-rich zone, in which the content of magnesium was not high. Combining these observations with the results of the XRD in Figure 8b, it could be inferred that the sword crystals were magnesium calcium silicate, while the needle crystals were calcium sodium silicate. The cross-section morphology of the coating after 100 h hot corrosion is shown in Figure 11d. In some locations where severe corrosion occurred, the coating thickness was reduced by 8 μm. In addition, there was white crystal enrichment and precipitation on the outside of the coating, which corresponded to the calcium sodium silicate and magnesium calcium silicate observed on the surface.
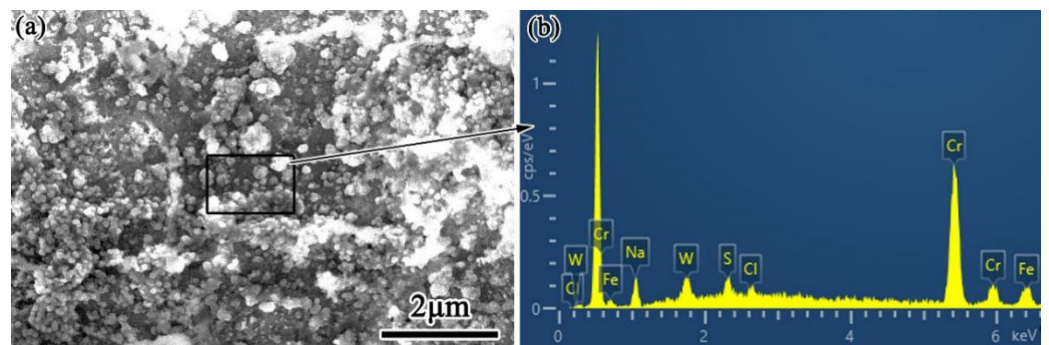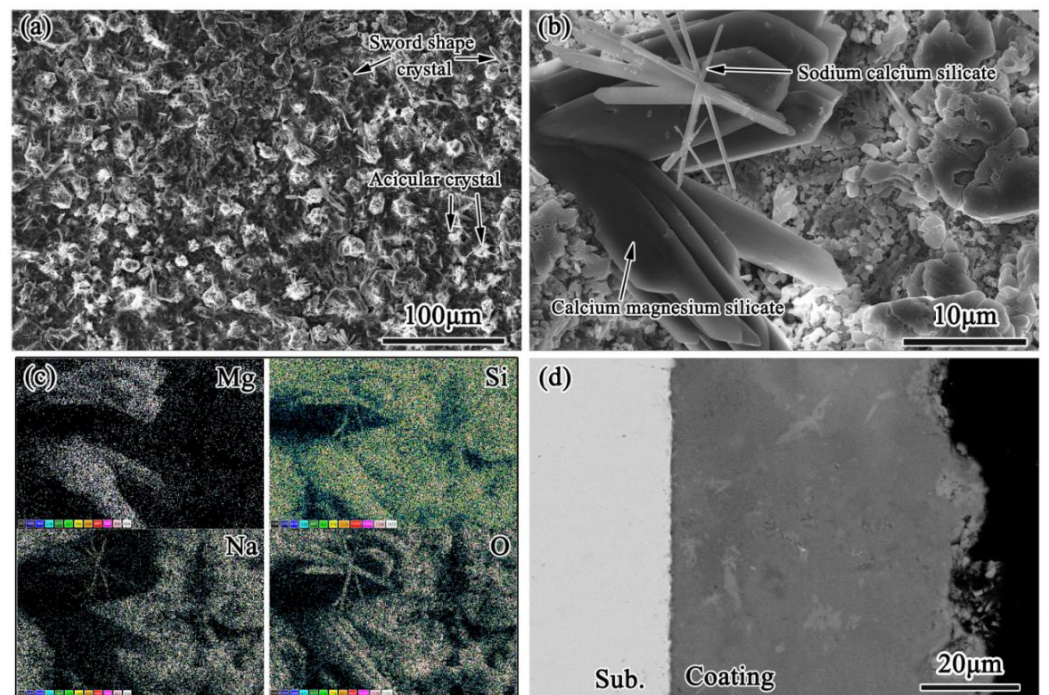

Figure 10. (**a**) Morphology and (**b**) elemental profile (analyzed by EDS) of the dissolved corrosion products precipitating from cleaning water.

Figure 11. Low-magnification morphology (**a**), high-magnification surface image (**b**), elemental map-scan profile (analyzed by EDS) (**c**), and cross-sectional image (**d**) of the MSS with GCC after 100 h oxidation at 650 °C.

4. Discussion

4.1. Oxidation and Hot Corrosion Mechanism of MSS at 650 °C

4.1.1. Oxidation Mechanism

The main oxidation reactions of MSS at 650 °C are as follows:

$$2Cr + 3/2\ O_2 = Cr_2O_3 \tag{1}$$

$$2Fe + 3/2\ O_2 = Fe_2O_3 \tag{2}$$

$$Fe + 1/2\ O_2 = FeO \tag{3}$$

Three standard Gibbs free energies of Reaction (1) at 650 °C is −891.0 kJ/mol, which is less than that of Reaction (2) (−578.6 kJ/mol) and Reaction (3) (−204.1 kJ/mol) at 650 °C. In other words, Cr_2O_3 is more stable than Fe_2O_3 and FeO at 650 °C from a thermodynamic point of view. That is to say, under the condition of the sufficient storage of Cr content in the substrate, oxide of iron will be reduced by the Cr diffused from the substrate [30].

For 1Cr11Ni2WMoV MSS, 11 wt.% Cr in the substrate provides sufficient Cr source to form a pure chromium oxide layer. The growth rate of Cr_2O_3 film is controlled by the transport of Cr ions through the growing oxide film. Moreover, Cr atoms possesses a rather low self-diffusion coefficient in Cr_2O_3 (only 1×10^{-14} cm^2/s at 1000 °C) [31]. Therefore, the Cr_2O_3 film on the MSS grows slowly and provides a satisfactory high temperature oxidation resistance at 650 °C, which can be proved by the results in Figures 3 and 5.

4.1.2. Hot Corrosion Mechanism

The eutectic temperature of NaCl and Na_2SO_4 is 630 °C. It is lower than the experimental temperature of 650 °C, indicating that under the experimental conditions, the coated salt film will melt into liquid. As a result, type I hot corrosion occurred on MSS [32].

A schematic illustration of the hot corrosion model of MSS covered by NaCl + Na_2SO_4 eutectic molten salt film is presented in Figure 12. The corrosion process can be divided into the following three stages:

Stage I: At high temperature, chromium oxide will be formed on the surface of the substrate. Competing with the growth of chromium oxide, Cl$^-$ ions in the molten salt will attack the chromium oxide [33], and the reaction formula is:

$$2Cl^- + Cr_2O_3 + 5/2\ O_2 = CrO_4{}^{2-} + Cl_2 \tag{4}$$
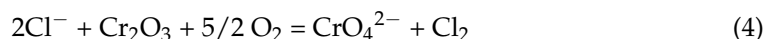
Meanwhile, the molten salt will diffuse to the surface of the substrate through the defects of the oxide and make direct contact with the matrix. In these locations, hot corrosion will occur following the acid fluxing model [34]: 1. The metal in the alloy will combine with O^{2-} ions in the molten salt to form corresponding oxides. 2. Refractory elements (W\Mo\V) will have a strong affinity with O^{2-} ions [32], resulting in the following reactions:

$$2WO_3 + O^{2-} = WO_4{}^{2-} \tag{5}$$

$$2MoO_3 + O^{2-} = MoO_4{}^{2-} \tag{6}$$

$$V_2O_5 + O^{2-} = 2VO_3{}^- \tag{7}$$

The above reactions consume the O^{2-} ions at the oxide/salt interface, and the molten salt at the interface becomes acidic, resulting in the acidic fluxing of oxide [34]:

$$FeO = Fe^{2+} + O^{2-} \tag{8}$$

$$Fe_2O_3 = 2Fe^{3+} + 3O^{2-} \tag{9}$$

$$2Cr_2O_3 = 2Cr^{3+} + 3O^{2-} \tag{10}$$

At the same time, $MoO_4{}^{2-}$, $Wo_4{}^{2-}$, $VO_3{}^-$, Fe^{3+}, Fe^{2+}, Cr^{3+} ions formed by Reactions (5)–(10) will diffuse from the oxide/salt interface to the salt/atmosphere interface. 3. In the

salt/atmosphere interface, MoO_4^{2-}, WO_2^-, VO_3^- ions will volatilize and release O^{2-} and Fe^{2+}, and Fe^{3+} ions will combine with them to form oxide again.

Stage II: Molten salt will continue to corrode not only at the depth, but preferably along the grain boundaries as well. Firstly, as the atoms at the grain boundary deviate from their equilibrium position, they have higher energy. Furthermore, the grain boundary has more defects. Lastly, the precipitation of chromium rich carbides at the grain boundary can easily lead to chromium depletion around the grain boundary. The above three factors will cause the area around the grain boundary to be easily corroded compared to the inside of the grain boundary. It is the intergranular corrosion that results in the morphology of metal-oxide mixed layer as shown in Figure 9b.

Stage III: During the process of salt cleaning, the soluble ion (such as CrO_4^{2-} and WO_4^{2+}) in the salt film will be washed away along with the salt, which is the reason why deionized water turns yellow and the significant signals of Cr and W can be detected in the crystal of soluble corrosion products (Figure 10b), leaving insoluble Fe_2O_3 and Fe_3O_4 attached to the alloy surface. On account of the loss of support and connection with salt, the loose oxides that form in the salt/atmosphere interface are easy to crack and peel off, as observed in Figure 9a, showing their powerlessness to prevent the intrusion of molten salt.
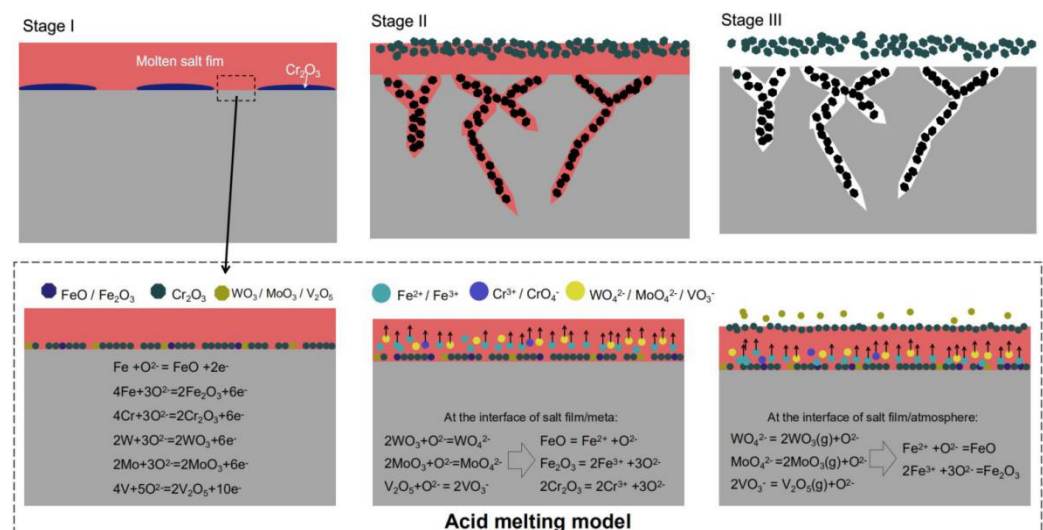
Figure 12. Schematic illustration of the hot corrosion model of MSS covered by NaCl + Na_2SO_4 eutectic molten salt film.

4.2. GCC Improves Oxidation Resistance of MSS at High Temperature

It is obvious from the kinetics that the GCC can significantly improve the oxidation resistance of MSS at 650 °C. The main reasons lie in the following two points:

I. Dense GCC impedes the diffusion of O^{2-} ions to the coating/substrate interface. Quartz, calcium silicate, and barium silicate crystals gradually precipitate from the glass phase of the coating during the oxidation at 650 °C. It is difficult for O^{2-} ions to diffuse in the silicate glass phase or in these silicate crystals. For example, the self-diffusion coefficient of oxygen in quartz is only 1.3×10^{-18} cm^2/s at 1000 °C [35]. Therefore, the diffusion of Cr atoms through the coating becomes the primary process of high temperature oxidation. As mentioned in the literature [36], Cr ions dissolved within the coating react with barium to form Ba_2CrO_4 crystal precipitation. The XRD patterns (Figure 4b) and the enrichment of Ba and Cr in the coating/substrate interface (Figure 6d) can prove this.

II. GCC promotes the selective oxidation of the chromium of MSS. When the glass melts on the surface of the substrate, the oxygen partial pressure decreases sharply, which promotes the selective oxidation of chromium oxide. Therefore, a dense chromium oxide layer forms rapidly at the coating/substrate interface. As the sample is placed in the

atmosphere at 650 °C, the Cr_2O_3 layer grows slowly and reacts with Ba^{2+} ions in enamel to form $BaCrO_2$. These results are in accord with those of recent studies [37]. As shown in Figure 6d, this layer was thinner and denser than the Cr_2O_3 layer formed in the atmosphere. This compact structure is very important for hindering the diffusion of cation and anion.

4.3. Hot Corrosion Behavior of GCC

The crystallization behavior of the GCC is significantly changed by the molten salt. According to the XRD patterns, the main precipitates in the GCC are quartz, calcium silicate, and barium silicate in an air atmosphere at 650 °C. After coating with $NaCl + Na_2SO_4$ film, the above crystals are no longer precipitated from glass, but sword-like magnesium calcium silicate and needle-like sodium calcium silicate crystals are precipitated. The reason for this phenomenon is the high concentration of Na^+ ions in the salt film. At a high temperature, driven by the concentration gradient, Na^+ ions will diffuse into the glass phase [38]. Because Na^+ ion is a strong flux, large amount of Na^+ ion infiltration will destroy the Si-O bond (bridging oxygen) in the glass phase [39]. As a matter of fact, the connection degree of the Si-O network is tremendously reduced, which makes it difficult to rearrange the silicon oxide tetrahedron [SiO_4] according to the trigonal system. This is why the precipitation of quartz crystal is inhibited. At the same time, because a large amount of sodium is infiltrated into the glass phase, it will promote the precipitation of sodium calcium silicate instead of calcium silicate crystals. Simultaneously, these crystals may become the nucleation sites of calcium magnesium silicate, promoting the precipitation of calcium magnesium silicate.

The molten salt reduces the high temperature resistance of GCC. As discussed above, sodium ions in the salt film will invade the glass phase, resulting in the fracture of the silica network, which will accelerate the physical dissolution of the glass into the salt film. After 20 h of corrosion, the salt film will be cleaned and replaced with fresh salt film, which means that the unsaturated salt film can continuously dissolve the glass phase. At the same time, the sodium-rich glass with loose silica network can easily dissolve into water during the salt cleaning process. The obvious thinning of GCC in Figure 11d proves this.

It should be noted that, in this study, we concentrate only on the oxidation and hot corrosion behavior of MSS with and without GCC in simulated conditions. In the practical environment, the behavior of GCC can be much more complex than in our experiment. Despite its preliminary character, this study clearly indicates that the GCC can greatly improve the oxidation and hot corrosion resistance of MSS.

5. Conclusions

Based on the above results and discussion, the following conclusions can be drawn:

1. Owing to the formation of Cr_2O_3 film, 1Cr11Ni2W2MoV martensitic stainless steel has good high temperature oxidation resistance at 650 °C.

2. When exposure in $NaCl$-Na_2SO_4 eutectic molten salt at 650 °C, loose and easily exfoliated iron oxide layers form on the martensitic stainless steel, which cannot prevent the invasion of corrosive medium. As a result, catastrophic intergranular corrosion occurs.

3. A dense glass-ceramic coating was successfully prepared on martensitic stainless steel. The coating can significantly reduce the oxidation rate of the substrate by promoting the selective oxidation of steel to form a compact chromium oxide film, reducing the diffusion rate of oxygen. By isolating the corrosive medium from the substrate, the coating notably improves the hot corrosion resistance of the substrate.

Author Contributions: All persons who have made substantial contributions to the work are ported in the manuscript. K.C. carried out most of the work. J.L., W.Z. and K.L. helped analyze the results and revised the manuscript. A.Y. and S.H. helped analyze the results and gave advice for the improvement of the work. W.L., M.C. and F.W. were responsible for the project design. All authors have read and agreed to the published version of the manuscript.

Data Availability Statement: Data is contained within the article.

Conflicts of Interest: The authors declare no conflict of interest.

References

1. Baddoo, R.N. Stainless steel in construction: A review of research, applications, challenges and opportunities. *J. Constr. Steel Res.* **2008**, *64*, 1199–1206. [CrossRef]
2. Huenert, D.; Kranzmann, A. Impact of oxyfuel atmospheres $H_2O/CO_2/O_2$ and H_2O/CO_2 on the oxidation of ferritic–martensitic and austenitic steels. *Corros. Sci.* **2011**, *53*, 2306–2317. [CrossRef]
3. Wood, G.C. The oxidation of iron-chromium alloys and stainless steels at high temperatures. *Corros. Sci.* **1962**, *2*, 173–196. [CrossRef]
4. Tsai, M.C.; Chiou, C.S.; Du, J.S.; Yang, J.R. Phase transformation in AISI 410 stainless steel. *Mater. Sci. Eng. A* **2002**, *332*, 1–10. [CrossRef]
5. Li, C.X.; Bell, T. Corrosion properties of plasma nitrided AISI 410 martensitic stainless steel in 3.5% NaCl and 1% HCl aqueous solutions. *Corros. Sci.* **2006**, *48*, 2036–2049. [CrossRef]
6. Sui, J.; Lehmusto, J.; Bergelin, M.; Hupa, L. Initial oxidation mechanisms of stainless steel Sanicro 28 (35Fe27Cr31Ni) exposed to KCl, NaCl, and K_2CO_3 under dry and humid conditions at 535 °C. *Corros. Sci.* **2019**, *155*, 29–45. [CrossRef]
7. Radhakrishnan, V.M.; Iyer, K.; Iyer, S. Hot corrosion cracking of stainless steel. *Mater. Corros.* **1982**, *33*, 461–466. [CrossRef]
8. Hiramatsu, N.; Uematsu, Y.; Tanaka, T.; Kinugasa, M. Effects of alloying elements on NaCl-induced hot corrosion of stainless steels. *Mat. Sci. Eng. A* **1989**, *120*, 319–328. [CrossRef]
9. Mesquita, T.J.; Chauveau, E.; Mantel, M.; Bouvier, N.; Koschel, D. Corrosion and metallurgical investigation of two supermartensitic stainless steels for oil and gas environments. *Corros. Sci.* **2014**, *81*, 152–161. [CrossRef]
10. Shi, L.; Xin, L.; Wang, X.; Wang, X.; Wei, H.; Zhu, S.; Wang, F. Influences of MCrAlY coatings on oxidation resistance of single crystal superalloy DD98M and their inter-diffusion behaviors. *J. Alloys Compd.* **2015**, *649*, 515–530. [CrossRef]
11. Tang, Z.; Wang, F.; Wu, W. Effect of a sputtered TiAlCr coating on the oxidation resistance of TiAl intermetallic compound. *Oxid. Met.* **1997**, *48*, 511–525. [CrossRef]
12. Shen, H.H.; Liu, L.; Liu, X.Z.; Guo, Q.; Meng, T.X.; Wang, Z.X.; Yang, H.J.; Liu, X.P. Zr/ZrC modified layer formed on AISI 440B stainless steel by plasma Zr-alloying. *Appl. Surf. Sci.* **2016**, *388*, 126–132. [CrossRef]
13. Dao-Xin, Y.T.L.; Han, D. Improvement of erosion and erosion–corrosion resistance of AISI420 stainless steel by low temperature plasma nitriding. *Appl. Surf. Sci.* **2008**, *254*, 5953–5958. [CrossRef]
14. Cambon, J.B.; Ansart, F.; Bonino, J.P.; Turq, V. Effect of cerium concentration on corrosion resistance and polymerization of hybrid sol–gel coating on martensitic stainless steel. *Prog. Org. Coat.* **2012**, *75*, 486–493. [CrossRef]
15. Li, W.; Zhu, S.; Wang, C.; Chen, M.; Shen, M.; Wang, F. SiO_2-Al_2O_3-glass composite coating on Ti-6Al-4V alloy: Oxidation and interfacial reaction behavior. *Corros. Sci.* **2013**, *74*, 367–378. [CrossRef]
16. Chen, M.; Shen, M.; Zhu, S.; Wang, F.; Niu, Y. Preparation and thermal shock behavior at 1000 °C of a glass-alumina-NiCrAlY tri-composite coating on K38G superalloy. *Surf. Coat. Technol.* **2012**, *206*, 2566–2571. [CrossRef]
17. Chen, M.; Shen, M.; Wang, X.; Zhu, S.; Wang, F. Oxidation and thermal shock behavior of a glass-alumina composite coating on K38G superalloy at 1000 °C. *J. Mater. Sci. Technol.* **2012**, *28*, 433–438. [CrossRef]
18. Wang, C.; Wang, W.; Zhu, S.; Wang, F. Oxidation inhibition of γ-TiAl alloy at 900 °C by inorganic silicate composite coatings. *Corros. Sci.* **2013**, *76*, 284–291. [CrossRef]
19. Xiong, Y.; Zhu, S.; Wang, F. The oxidation behavior and mechanical performance of Ti60 alloy with enamel coating. *Surf. Coat. Technol.* **2005**, *190*, 195–199. [CrossRef]
20. Zheng, D.; Zhu, S.; Wang, F. Oxidation and hot corrosion behavior of a novel enamel-Al_2O_3 composite coating on K38G superalloy. *Surf. Coat. Technol.* **2006**, *200*, 5931–5936. [CrossRef]
21. Shen, M.; Zhu, S.; Xin, L.; Wang, F. Hot Corrosion Behavior of a Novel Enamel-Based Thermal Barrier Coating. *Mater. Sci. Forum.* **2010**, *654–656*, 1944–1947. [CrossRef]
22. Li, W.; Chen, M.; Wang, C.; Zhu, S.; Wang, F. Preparation and oxidation behavior of SiO_2-Al_2O_3-glass composite coating on Ti-47Al-2Cr-2Nb alloy. *Surf. Coat. Technol.* **2013**, *218*, 30–38. [CrossRef]
23. Li, W.; Chen, M.; Wang, C.; Zhu, S.; Wang, F. Glass–ceramic coatings on titanium alloys for high temperature oxidation protection: Oxidation kinetics and microstructure. *Corros. Sci.* **2013**, *74*, 178–186. [CrossRef]
24. Liao, Y.; Zhang, B.; Chen, M.; Feng, M.; Wang, J.; Zhu, S.; Wang, F. Self-healing metal-enamel composite coating and its protection for TiAl alloy against oxidation under thermal shock in NaCl solution. *Corros. Sci.* **2020**, *167*, 108526. [CrossRef]

25. Liu, Y.R.; Dong, Y.E.; Yong, Q.L.; Jie, S.U.; Zhao, K.Y.; Jiang, W. Effect of Heat Treatment on Microstructure and Property of Cr13 Super Martensitic Stainless Steel. *J. Iron Steel. Res.* **2011**, *18*, 60–66. [CrossRef]

26. Zhang, L.; Schmetterer, C.; Masset, P.J. Thermodynamic description of the M_2O–SiO_2 (M=K, Na) systems. *Comput. Mater. Sci.* **2013**, *66*, 20–27. [CrossRef]

27. Goel, A.; Tulyaganov, D.U.; Ferrari, A.M.; Shaaban, E.R.; Prange, A.; Bondioli, F.; Ferreira, J.M.F. Structure, Sintering, and crystallization kinetics of alkaline-earth aluminosilicate glass–ceramic sealants for solid oxide fuel cells. *J. Am. Ceram. Soc.* **2010**, *93*, 830–837. [CrossRef]

28. Yu, Z.; Chen, M.; Shen, C.; Zhu, S.; Wang, F. Oxidation of an austenitic stainless steel with or without alloyed aluminum in O_2+10% H_2O environment at 800 degrees C. *Corros. Sci.* **2017**, *121*, 105–115. [CrossRef]

29. Fujikawa, H. Review of several studies on high temperature oxidation behaviour and mechanism of austenitic stainless steels. *Defect Diff. Forum.* **2011**, *312–315*, 1097–1105. [CrossRef]

30. Ostwald, C.; Grabke, H.J. Initial oxidation and chromium diffusion. I. Effects of surface working on 9–20% Cr steels. *Corros. Sci.* **2004**, *46*, 1113–1127. [CrossRef]

31. Sabioni, A.; Huntz, A.M.; Philibert, J.; Lesage, B.; Monty, C. Relation between the oxidation growth rate of chromia scales and self-diffusion in Cr_2O_3. *J. Mater. Sci.* **1992**, *27*, 4782–4790. [CrossRef]

32. Pettit, F. Hot Corrosion of Metals and Alloys. *Oxid. Met.* **2011**, *76*, 1–21. [CrossRef]

33. Rapp, R.A.; Zhang, Y.S. Hot corrosion of materials: Fundamental studies. *JOM* **1994**, *46*, 47–55. [CrossRef]

34. Rapp, R.A. Hot corrosion of materials: A fluxing mechanism? *Corros. Sci.* **2002**, *44*, 209–221. [CrossRef]

35. Takahashi, T.; Fukatsu, S.; Itoh, K.M.; Uematsu, M.; Shiraishi, K. Self-diffusion of Si in thermally grown SiO_2 under equilibrium conditions. *J. Appl. Phys.* **2003**, *93*, 3674–3676. [CrossRef]

36. Feng, M.; Chen, M.; Yu, Z.; Chen, Z.; Wang, F. Crystallization and wear behavior of SiO_2-Al_2O_3-ZrO_2-Ba(Sr, Ca)O glass-ceramics added with Cr_2O_3 by different methods. *Ceram. Int.* **2019**, *45*, 22617–22624. [CrossRef]

37. Chen, M.; Li, W.; Shen, M.; Zhu, S.; Wang, F. Glass coatings on stainless steels for high-temperature oxidation protection: Mechanisms. *Corros. Sci.* **2014**, *82*, 316–327. [CrossRef]

38. Gy, R. Ion exchange for glass strengthening. *Mat. Sci. Eng. B* **2008**, *149*, 159–165. [CrossRef]

39. Greaves, G.; Fontaine, A.; Lagarde, P.; Raoux, D.; Gurman, S. Local Structure of Silicate Glass. *Nature* **1981**, *293*, 611–616. [CrossRef]